

RESEARCH ARTICLE

10.1029/2020JA028995

Key Points:

- Two-azimuth co-seismic ionospheric disturbances (CIDs) are found from Global Positioning System observations following the 2020 Jamaica earthquake
- The CIDs are mainly triggered by the upward propagating secondary acoustic wave by the seismic Rayleigh wave
- The co-seismic ionospheric disturbances display different polarity and amplitude characteristics due to the fault system

Correspondence to:

S. Jin,
sgjin@shao.ac.cn;
sg.jin@yahoo.com

Citation:

Chai, Y., & Jin, S. (2021). Two-azimuth co-seismic ionospheric disturbances following the 2020 Jamaica earthquake from GPS observations. *Journal of Geophysical Research: Space Physics*, 126, e2020JA028995. <https://doi.org/10.1029/2020JA028995>

Received 2 DEC 2020
Accepted 25 AUG 2021

Two-Azimuth Co-Seismic Ionospheric Disturbances Following the 2020 Jamaica Earthquake From GPS Observations

Yi Chai^{1,2} and Shuanggen Jin¹ 

¹Shanghai Astronomical Observatory, Chinese Academy of Sciences, Shanghai, China, ²University of Chinese Academy of Sciences, Beijing, China

Abstract Co-seismic ionospheric disturbance (CID) may provide insights on understanding the coupled nature of earthquake–atmosphere geophysical processes. In this study, the CIDs following the M_w 7.7 Jamaica earthquake on January 28, 2020 are detected about 12 min after the main shock by the dual-frequency Global Positioning System measurements. Significant CIDs at two azimuths are observed from satellite PRN03, 04 and 26 with spreading out at 3.54, 3.51 and 3.48 km/s respectively, which are close to the spreading speeds of Rayleigh waves recorded by the seismographs. The significant CID signals are found in south near-field area and southwest far-field area. Furthermore, CID characteristics are analyzed in terms of amplitude, elevation and azimuth angle, waveform, and frequency domain. Results show that CIDs are observed by PRN03, 04 and 26 at low elevation angles ($<35^\circ$) in infrasonic wave frequency domain and the average negative amplitudes of CIDs observed by PRN26 are larger than -0.08 TECU, while the CID amplitudes observed by PRN03 and PRN04 are about -0.05 and -0.07 TECU, respectively. Moreover, the azimuthal asymmetry of CID amplitude in SW and SE azimuths and different initial polarities in disturbance signals are found and discussed from tectonic and nontectonic factors. The relations among CID, Rayleigh wave and focal mechanism are interpreted. The upward propagating secondary acoustic wave triggered by the seismic Rayleigh wave from earthquake is the main source of CIDs. These results confirm that strike-slip earthquake can also generate pronounced co-seismic ionospheric disturbances.

1. Introduction

Earthquakes are common natural disasters (Jin & Park, 2006). During the main shock of earthquakes, the rupture and severe co-seismic vertical crust movements can excite acoustic resonance, and some of the acoustic resonance can propagate upward into the ionosphere in the form of acoustic waves and induce variations of the ionospheric total electron content (TEC), which is the so-called ionospheric disturbances (Jin et al., 2011, 2015). The ionospheric disturbances were related to the acoustic-gravity wave launched by big earthquakes (Ronald, 1966, 1967). The first ionosphere disturbance was detected by Leonard and Barnes (1965) using the ionospheric vertical sounding following the great Alaska earthquake in 1964. Davies and Baker (1965) found the frequency oscillations in radio signals following the same Alaska earthquake. Later more co-seismic ionospheric disturbances (CIDs) were reported with great attentions together understanding the mechanism of earthquakes and crust vertical movement.

However, due to the limitation of the measurement instruments in the last few decades, it is difficult to investigate the detailed characteristics of CID and coupling process between the ground motion and the ionosphere (Okoh et al., 2018). Nowadays, dense Global Navigation Satellite System (GNSS) network observations can estimate the ionosphere and CID (Calais & Minster, 1995; Jin & Su, 2020; Jin et al., 2015) with its strong imaging capability, high spatial resolution and sensibility for detecting Rayleigh wave in the ionosphere (Ducic et al., 2003; Occhipinti et al., 2010). With the wide use of GNSS, the properties of CID and the relationship among CID, earthquake and ionosphere will be better understood. By estimating the ionospheric delays from Global Positioning System (GPS) (Jin et al., 2004), the TEC can be precisely calculated so that the seismic ionospheric anomaly related to the earthquake can be detected from the GPS-TEC time series observation (Jin, Jin, & Kutoglu, 2017; Jin et al., 2004). It will provide a chance to investigate the complete process and the properties of the earthquake, after estimating the CID signal. Moreover, as the

short time for CID wave to the ionosphere (around 8 min), CID will have potential in realizing near-real-time earthquake monitoring and early tsunami warning (Astafyeva, 2019; Komjathy et al., 2016; Rolland et al., 2010).

Nowadays, a number of studies have been performed to study the ionospheric disturbance induced by great earthquakes and provided a clear understanding of CIDs characteristics. For example, Afraimovich et al. (2010) found the intense N-shaped shock-acoustic waves that propagated to the ionosphere and induced the disturbance with a plane waveform following the 2008 Wenchuan earthquake. The CIDs in the far-field following the 2008 Wenchuan earthquake were perpendicular to the direction of the fault rupture (NE-SW) (Zhao & Hao, 2015). The far-field CID following the 2015 M_w 7.8 Nepal earthquake was detected by GPS-TEC observation up to 3,000 km from the epicenter (H. Liu et al., 2021) as the acoustic gravity wave induced by Rayleigh surface wave propagated into the ionosphere and caused the electronic and plasma density oscillation (Sripathi et al., 2020). Also, after the 2011 M_w 9.0 Tohoku Earthquake in Japan, significant ionospheric disturbance was investigated from nationwide GPS receiving networks and the disturbance was confirmed with three different propagation velocities, which attributed to three different generation sources (J. Y. Liu et al., 2011; Saito et al., 2011; Tsugawa et al., 2011). The phenomena of CIDs with different speeds have been found for other earthquakes. For example, Astafyeva et al. (2009) found two-mode long-distance CIDs following the great 1994 Kurile earthquake and the two-mode ionospheric disturbances with two different propagation velocities were detected and estimated following the 2005 Northern California offshore earthquake (Jin, 2018).

Whereas, there are still some problems and difficulties in investigating CID. For instance, the distinct TEC anomaly can be detected by GPS measurement only for some earthquakes with large magnitudes ($M_w > 6.5$) (Perevalova et al., 2014), as the large vertical crustal displacement and magnitude have important influences on the amplitude of CID (Astafyeva et al., 2013). Uneven distribution of ground-based GPS network makes the absence of ionospheric disturbance in some seismic regions. Besides, the directivity and coupling mechanism between CIDs and earthquakes are still not clear. Because the coupling process of earthquake-atmosphere-ionosphere and the characteristics of CID, such as amplitude, propagation speed and directivity (Heki & Ping, 2005), are controlled by earthquake parameters such as magnitude and focal mechanism (Astafyeva et al., 2009; Heki et al., 2006), the pattern of rupture and ground deformation (Afraimovich et al., 2010), and nontectonic forcing mechanisms in terms of geomagnetic field (Heki & Ping, 2005; Rolland et al., 2011, 2013), geometry of GPS line-of-sight signal (Afraimovich et al., 1998, 2001; Astafyeva et al., 2014) and ambient electron density gradient (Bagiya et al., 2019). Consequently, abundant investigations of CIDs following different earthquake events are necessary to comprehend the seismic motion process and coupling mechanism of earthquake-atmosphere-ionosphere.

In this paper, the CIDs are estimated and investigated following the $M_w = 7.7$ Jamaica earthquake on January 28, 2020 from the dense GPS network observations. In Section 2, data and methods are introduced, results and discussion are presented in Section 3, and finally conclusion is given in Section 4.

2. Data and Method

2.1. 2020 M_w 7.7 Earthquake

The 2020 M_w 7.7 earthquake occurred in the Caribbean Sea to the northwest of Jamaica, with 10 km in depth at 19:10:22 (UTC), January 28, 2020, as the result of the strike-slip faulting on the plate boundary between the North America and Caribbean Plates. The epicenter (19.46°N, 78.79°W) was located at the plate boundary and the fault plane struck along with the orientation of the plate boundary. The GPS observation data with a sampling rate of 15 s was obtained from dense University Navstar Consortium (UNAVCO) GPS stations.

The distributions of 112 GPS stations and 13 seismographs are shown in Figure 1 with the blue triangles and red dots, respectively. The data of seismometers was provided by Incorporated Research Institutions for Seismology (IRIS, http://ds.iris.edu/wilber3/find_stations/11176800). The red pentagram represents the epicenter of the 2020 M_w 7.7 earthquake and the black line represents the fault plane near the epicenter. The beach ball indicates the focal mechanism of the earthquake event at the upper-right corner of the figure. Magnetic field (MF) parameters in height = 350 km involving inclination (I) and declination (D) are shown

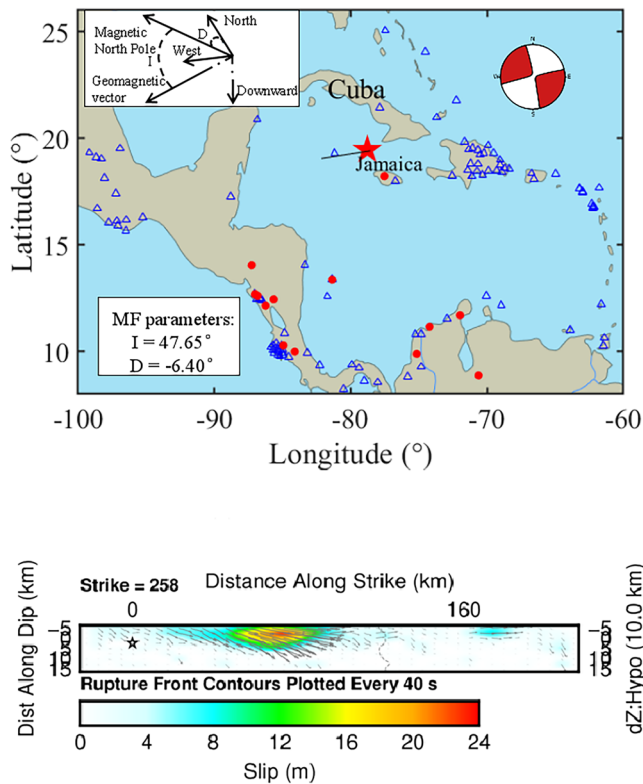


Figure 1. The seismic information of the M_w 7.7 Jamaica earthquake and distribution of Global Positioning System (GPS) dense network stations and seismographs around the epicenter area and geomagnetic information about the earthquake (a). The blue triangles and red dots denote the location of GPS stations and seismographs, respectively. The focal mechanism is obtained from U.S. Geological survey (USGS, <https://earthquake.usgs.gov/earthquakes/eventpage/pt20028001/moment-tensor>) (b). The slip distribution map was obtained from USGS (<https://earthquake.usgs.gov/earthquakes/eventpage/us60007idc/executive>).

in the white panel at lower-left quarter. The schematic view of magnetic field plotted in arrows is shown in the white panel at the upper-left corner of Figure 1a. The slip distribution map of the 2020 M_w 7.7 Jamaica earthquake is shown in Figure 1b. Related information (finite fault and slip distribution) of this earthquake event is accessible from U.S. Geological survey (USGS). The slip distribution map indicates the location and motion direction of fault plane in strike of 258° with arrows and the horizontal co-seismic displacement in color.

2.2. Method

The CID can be extracted from GPS-TEC time series. When GPS satellite signals propagate into the ionosphere, the ionospheric delay is related to the GPS signal frequency and ionospheric TEC. In order to obtain the ionospheric disturbances, the ionospheric TEC should be calculated precisely from the dual-frequency GPS observation ($f_1 = 1,575.42$ MHz, $f_2 = 1,227.60$ MHz) by the following equation (Brunini & Azpilicuetta, 2009; Jin, Jin, & Kutoglu, 2017; Jin, Jin, & Li, 2017; Jin et al., 2004):

$$\text{STEC} = \frac{f_1^2 f_2^2}{40.3(f_1^2 - f_2^2)} (L_1 - L_2 + \lambda_1(N_1 + b_1) - \lambda_2(N_2 + b_2) + \varepsilon_L) \quad (1)$$

$$\text{STEC} = \frac{f_1^2 f_2^2}{40.3(f_1^2 - f_2^2)} (P_1 - P_2 - (d_1 - d_2) + \varepsilon_p)$$

where STEC is the slant total electron content, L_1 and L_2 are the GPS carrier phase measurements in frequency f_1 and f_2 , P_1 and P_2 are the GPS code measurements in frequency f_1 and f_2 , λ_1 and λ_2 are the GPS signal wavelength in frequency f_1 and f_2 , N is the ambiguity, b is the instrument biases for carrier phase, d_1 and d_2 are the differential code biases, and ε is the residual. STEC represents the absolute magnitude of ionospheric TEC. In order to get the relative variation of the ionospheric TEC and estimate the characteristics of CID, the STEC along the GPS line of sight (LOS) is converted to vertical TEC (VTEC) by the following mapping function:

$$\text{VTEC} = \text{STEC} * \cos \left[\arcsin \left(\frac{R \sin(z)}{R + H} \right) \right] \quad (2)$$

where H is the height of the ionosphere shell, where H is assumed at 350 km of altitude. R is the Earth's radius, and z is the elevation angle of the satellite. The cycle slip is the main error in obtaining high-precision TEC values from above method (Nguyen et al., 2019). Therefore, the second-order time-difference phase ionospheric residual was used to eliminate cycle slip (Cai et al., 2013). Here the Butterworth filter of a fourth-order zero-phase finite impulse was used to remove the background noise and obtain the filtered TEC series. According to the Nyquist sampling theory, the Nyquist frequency is larger than 8 mHz for GPS observation as the sampling interval of GPS observation data is 15 s. The 2 mHz is the cutoff frequency of the acoustic above the ionospheric height. The GPS-TEC time series obtained from station LMNL and satellite PRN26 with different passband frequencies are shown in Figure 2. The distinct CID can be obtained from the series with the 2–5 mHz passband frequency filtering at about 12 min after the occurrence of the earthquake in the red line marked zone, so the fourth-order zero-phase Butterworth filter with passband frequency of 2 and 5 mHz was applied to obtain the CID time series.

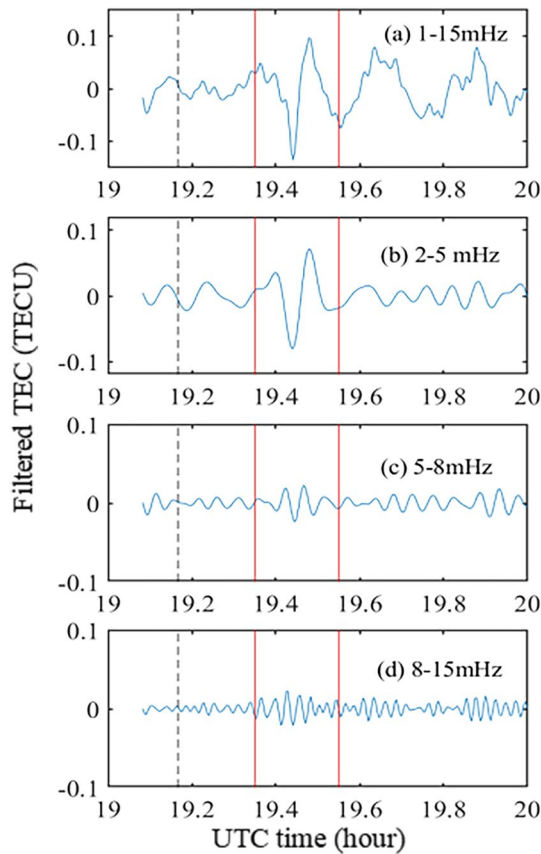


Figure 2. Global Positioning System-total electron content (TEC) time series obtained from station LMNL and satellite PRN26 with different filter passband frequencies. (a) Filtered TEC series with 1–15 mHz passband. (b) Filtered TEC series with 2–5 mHz passband. (c) Filtered TEC series with 5–8 mHz passband (d) Filtered TEC series with 8–15 mHz passband. The dashed black line represents the onset time of the 2020 Jamaica earthquake.

teristics of CID were estimated and discussed. The most pronounced ionospheric disturbances were detected by GPS satellites PRN03, PRN04 and PRN26. Figure 4 shows the traveling-time diagrams of CIDs and SIP tracks during 19:10–19:30 UTC. The SIP tracks diagrams show that SIP tracks with CID signals mainly cover the southeast, south and southwest area (Figure 3). The traveling-time diagrams demonstrate the linear relationship between the CID travel time and distance from SIP to the epicenter. The horizontal and vertical axes correspond to the UTC time and the distance between SIP and epicenter, respectively. The color of curves indicates the amplitude of filtered TEC series. The color bar denotes the variation range of filtered TEC (dTEC, in TECU, from -0.08 to 0.08 TECU). Significant traveling CID can be found through color variance in traveling-time diagrams 250–500, 500–700 and 300–800 km away from the epicenter, respectively. Moreover, the CID captured by PRN26 has the largest TEC negative amplitude, larger than -0.08 TECU, while the negative amplitude of CID detected by PRN03 and PRN04 only reaches to -0.05 TECU and -0.07 TECU, respectively. This indicates that these CIDs may have different amplitude characteristics. After performing the linear fit, the propagation velocities of the CIDs captured by PRN03, 04 and 26 are about 3.54, 3.51 and 3.48 km/s, respectively. The ionospheric disturbance generated by different sources can be distinguished through the velocities of their propagation. These velocities are larger than the sound speed at the ionospheric altitude (~ 1 km/s) and close to the Rayleigh surface wave propagation speed along the ground surface at 3,000–4,000 m/s (Astafyeva et al., 2014). According to Jin (2018), these ionospheric disturbances are probably the secondary acoustic wave generated by seismic Rayleigh waves with dynamic coupling.

3. Results and Discussion

3.1. Co-Seismic Ionospheric Disturbances

The CIDs following the 2020 Jamaica earthquake were detected and estimated. Figure 3 shows the TEC distribution maps during 19:10–19:30 UTC. The red pentagram represents the epicenter and the dots in color correspond to the location of subionospheric points (SIPs). The color value shows the TEC variation amplitude of SIPs and the color bar indicates the variation range of filtered TEC series (dTEC, in TECU, from -0.1 to 0.1 TECU). The 2020 Jamaica earthquake occurred at 19:10 UTC. Obvious ionospheric anomalies spreading out from the epicenter are first detected at the south near-field region of epicenter (200–450 km away from the epicenter, Figure 3b), after about 12 min of the main shock. Most of the TEC disturbances display in positive anomalies. The average amplitude reaches to 0.06 TECU ($1 \text{ TECU} = 10^{16} \text{ e/m}^2$). Around 2 min later at 19:24 UTC, the TEC disturbances become stronger and the amplitude reaches about -0.07 TECU at this time. It should be noted that the TEC disturbances turn positive anomalies to negative anomalies in the near field (Figure 3c). Besides, in the southwest far field (marked by red circle), there are slight positive disturbances. The negative TEC anomalies last for around 2 min and turn back to positive anomalies in the south near-field area at 19:26 UTC (Figure 3d) and the southwest far-field TEC disturbances turn slight positive anomalies to obvious negative anomalies. The average amplitude of near-field TEC disturbances is about 0.06 TECU, while the far-field TEC disturbances is about -0.07 TECU. After the same time interval as the previous discussed TEC disturbance (2 min), the TEC anomalies can be detected only in the southeast region (Figure 3e). After 19:30 UTC, no obvious TEC disturbances can be detected in the seismic region.

3.2. CID in Different Azimuths

The propagation characteristics of CIDs were further analyzed in the pattern, modes, generation mechanism and source of CIDs. In Section 3.1, the CIDs following the Jamaica earthquake have been detected though GPS-TEC observation. In this section, the generation source and characteristics of CID were estimated and discussed.

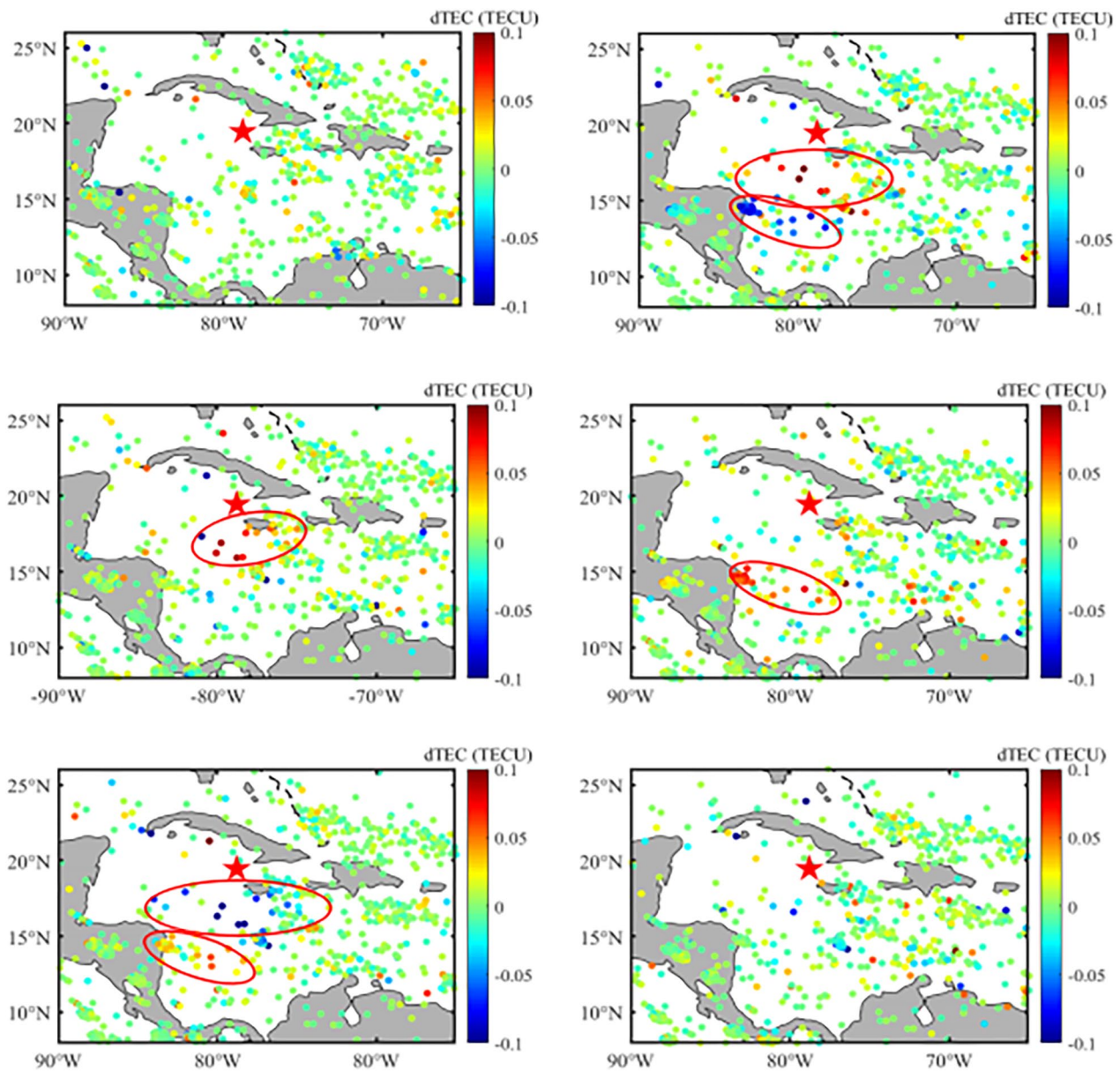


Figure 3. Filtered total electron content (TEC) distribution maps extracted from Global Positioning System observation data during 19:10–19:30 UTC. The red pentagram represents the epicenter and the color filled dots indicate the positions of subionospheric points. The color bar is the variation range of filtered TEC (dTEC, in TECU).

Figure 5 shows maximum amplitudes of the TEC-CID time series obtained from PRN03, 04 and 26 during 19:10–19:30 UTC when the CIDs appeared. The horizontal and vertical axes correspond to the elevation angle along the LOS between satellites and GPS stations and the ionospheric piercing point (IPP) epicentral azimuth, respectively. The color in these dots indicates the value of the maximum amplitude. As is shown in Figure 5a, the dots with the maximum larger than 0.03 TECU are mainly at the elevation angles 20–30°. In Figure 5b, the dots are mainly at elevation angles 28–32°, while the dots gather in elevation angles 28–35° in Figure 5c. All these elevation angles are lower than 40°, which is favorable to detect the Rayleigh wave-induced CID (Rolland et al., 2011). According to previous work (Afraimovich et al., 1998, 2001; Astafyeva et al., 2014), lower elevation angle can enlarge the horizontal extent of the ionospheric disturbance. As Rayleigh wave-induced CID waves propagate along nearly vertical direction into the ionosphere (Rolland et al., 2011), so when the satellite-to-receiver LOS is perpendicular to the disturbance wave vector, the

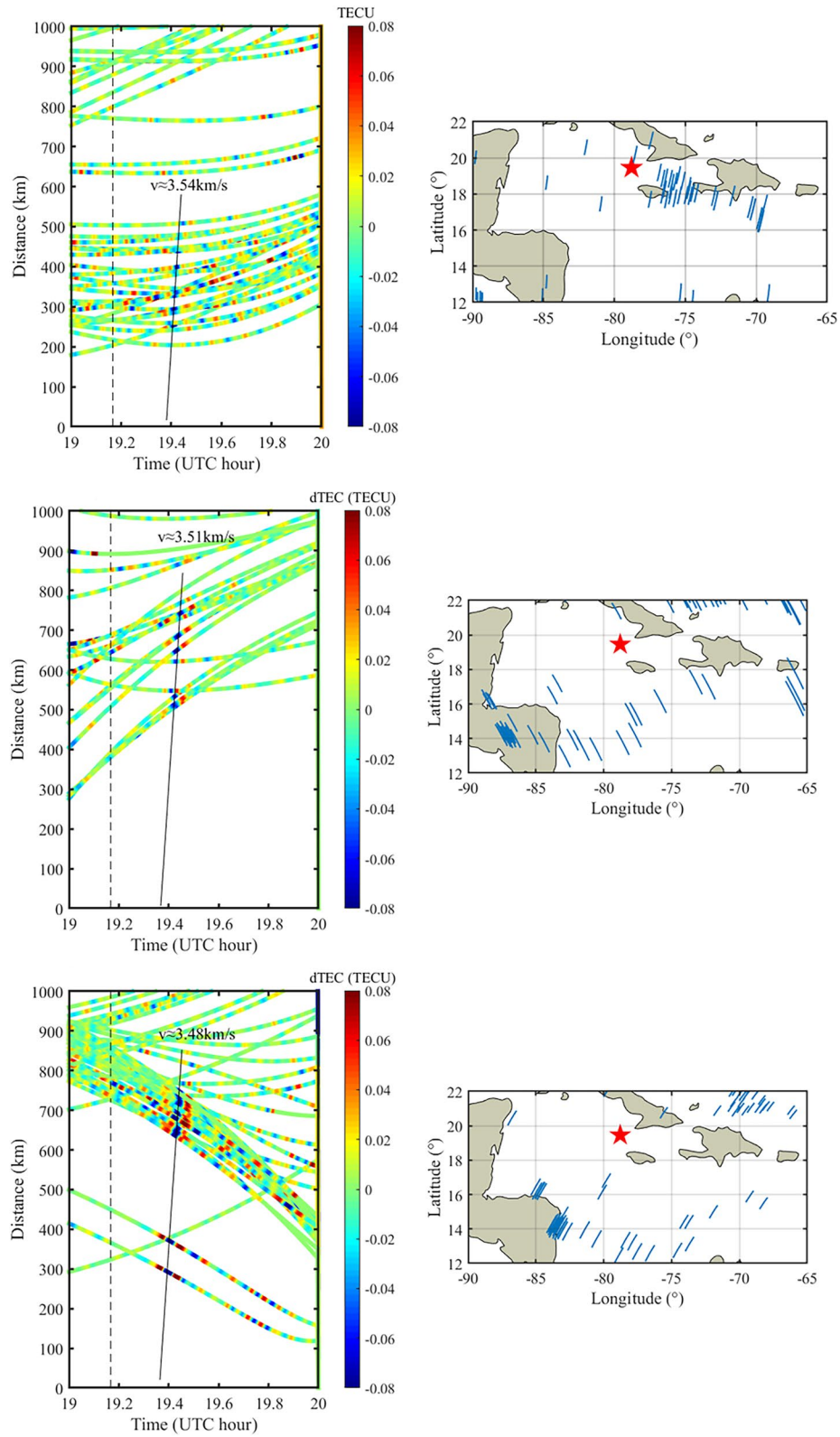


Figure 4.

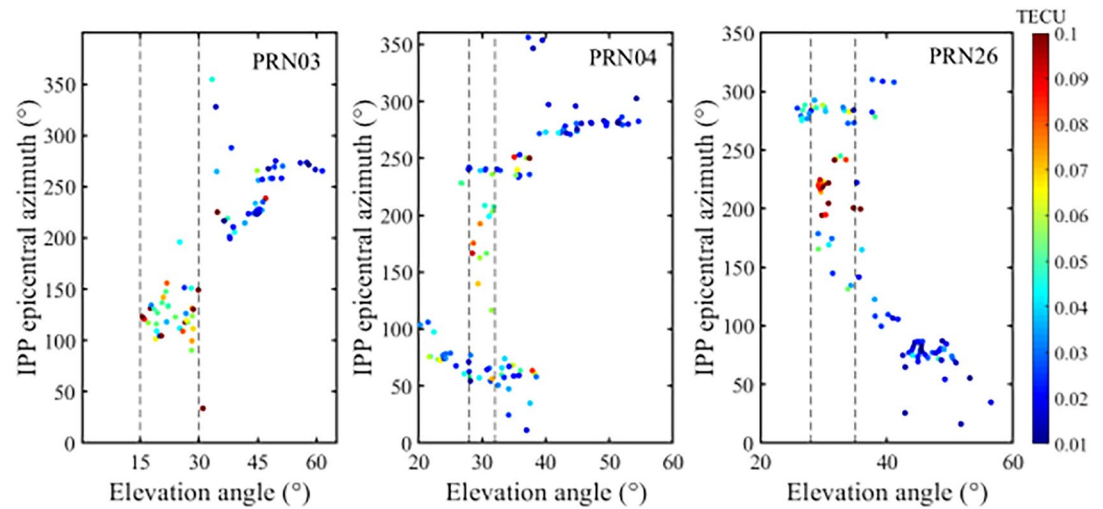


Figure 5. (a) Distribution of ionospheric piercing point (IPP) epicentral azimuths and elevation angles of the maximum in filtered total electron content (TEC) series obtained from PRN03. (b) Distribution of IPP epicentral azimuths and elevation angles of the maximum in filtered TEC series obtained from PRN04. (c) Distribution of IPP epicentral azimuths and elevation angles of the maximum in filtered TEC series obtained from PRN26. The dashed black lines marked the elevation angles range of the maximum amplitude larger than 0.03 TECU. The maximums of filtered TEC less than 0.01 TECU are neglected.

observed amplitude reaches its largest amount. On the other hand, the amplitude of the disturbance signal is relevant to the satellite elevation angle (Heki et al., 2006).

Figure 6 shows the azimuthal distribution of the average maximum amplitudes for all the filtered TEC time series obtained from PRN03, 04 and 26 in every 15° azimuth bin during 19:10–19:30 UTC in the form of polar diagram. The theta axis represents the epicenter azimuth (in degree). The radius axis stands for the average maximum amplitudes of filtered GPS-TEC series (in TECU). The north direction is set as the 0° azimuth. The maximums of filtered TEC less than 0.015 TECU are neglected. Obvious azimuthal asymmetry in maximum of TEC series can be seen in this diagram. Specifically, the average maximum amplitudes observed in southwest are equal to or greater than 0.06 TECU, which are larger than the average maximum amplitudes in southeast region (lower than 0.04 TECU). The average maximum amplitudes observed in southwest are close to the fault rupture region (azimuth angle 258°).

3.3. CID Waveform and Spectrum Signal

The spectrum analysis of the filtered GPS-TEC time series can provide more information about the CID. Figure 7 shows some cases of disturbance signal waveforms and seismic waveforms in different azimuthal directions. Disturbance waveforms observed by PRN03, 04 and 26 are shown in Figures 7a–7c, respectively. The x-axis represents the UTC time. The dashed black lines in Figures 7a–7c represent the onset time of the earthquake and the name of selected station is located in the right side of each corresponding waveform. The significant TEC disturbances can be distinguished from the waveforms after about 12 min of the main shock. As the distance between selected station and epicenter increases, the amplitude of waveforms becomes to decrease in Figure 7c, and the appearance time of negative peak begins to delay in Figures 7a–7c. It is notable that, in Figure 7c, the signals observed by station CN35 and SAN0 show a typical N-shape waveform. However, as the distance from epicenter increases, the waveforms observed by far-field station

Figure 4. Traveling-time diagrams of co-seismic ionospheric disturbance (CID) and graphs of subionospheric point (SIP) tracks distribution through Global Positioning System observation for PRN03, 04 and 26. (a) Traveling-time diagram of CID observed from PRN03 and SIP tracks for PRN03. (b) Traveling-time diagram of CID observed from PRN04 and SIP tracks for PRN04. (c) Traveling-time diagram of CID observed from PRN26 and SIP tracks for PRN26. Dashed black line represents the onset time of the 2020 Jamaica earthquake. The color bars indicate the value range of filtered total electron content (TEC) series. The black diagonal line is used to linearly fit the propagation velocity of TEC disturbances. The red pentagram and the blue lines in SIP tracks distribution graphs represent the epicenter and SIP tracks during 19:10–19:30 UTC, respectively.

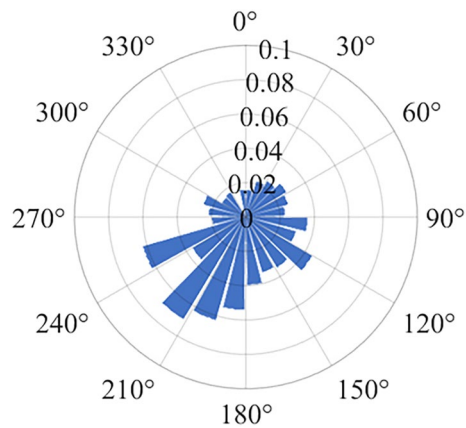


Figure 6. The polar diagram for the distribution of the average maximum amplitude for all the filtered Global Positioning System-total electron content (TEC) time series obtained from PRN03, 04 and 26 in every 15° azimuth bin during 19:10–19:30 UTC. The theta axis represents the subionospheric point epicenter azimuth of the maximum TEC series (in degree). The radius axis stands for the average maximum amplitudes of filtered TEC series (in TECU). The north direction is set as the 0° azimuth. The maximums of filtered TEC less than 0.015 TECU are neglected.

LMNL, PUMO, LEPA, PUJE, HUA2 and GRZA appear in the form of an inverted N-shaped waveform (Astafyeva et al., 2013). In Figure 7a, all the waveforms have N type forms, which are different from the waveforms of selected stations with PRN26. Besides, the inverted N-shaped waveform and N-shape waveform both appear in the signal observed from PRN04. With the same passband filtering, the seismic waveforms at 2–5 mHz in southeast and southwest direction from the vertical broadband high-gain seismometers are shown in Figures 7d and 7e respectively. The amplitude of waveforms represents the normalized vertical ground displacement. The y-axis represents the distance between seismograph and epicenter and the x-axis indicates UTC time. It is apparent that the vertical displacements in SW direction are larger than SE direction. Through linearly fitting, the spread speed of seismic waves in southwest direction is about 3.75 km/s, which is close to the speed 3.76 km/s in southeast direction. These two propagation speeds are both in the velocity range of Rayleigh surface wave and close to the propagation velocities of CID described in Figure 4. This confirms that the CIDs are the secondary acoustic waves generated by seismic Rayleigh waves with dynamic coupling. Besides, it should be noticed that the seismic waves in SW show a negative polarity, which are consistent with the inverted N-shape waveforms of Rayleigh wave-induced ionospheric disturbances observed by PRN26 in the southwest area. The same result can be obtained by comparing Figures 7a and 7d.

Furthermore, Figure 8 shows the spectrograms of the filtered GPS-TEC time series from selected stations and satellites after using short-time Fourier transform (STFT) to convert TEC series from the time domain to the frequency domain. The diagram order is station CN35 for PRN26, station HUA2 for PRN26, station JME2 for PRN03 and station RDMS for PRN03 respectively. The left panel displays the filtered GPS-TEC time series in blue line and distance changes in orange line, and the right panel represents the spectrogram of corresponding GPS-TEC time series converting from STFT. The center frequencies of disturbance signals for station CN35 and station GRZA are about 3.4 and 3 mHz respectively, while frequencies of disturbance signals for station JME2 and station RDMS are centered at about 3.3 and 3.1 mHz. The center frequencies for selected stations are all in the frequency range of infrasonic wave. Therefore, these CID signals have the same frequency characteristic.

3.4. Discussion

The eruption of the 2020 Jamaica strike-slip earthquake excited seismic Rayleigh surface waves that induced the upward secondary acoustic waves with dynamic coupling and caused TEC fluctuation in the ionosphere height. The distinct CIDs were captured by GPS observation (mainly PRN03, PRN04 and PRN26) after about 12 min of the main shock. This demonstrates that the strike-slip Jamaica earthquake can also cause co-seismic ionospheric disturbance (Astafyeva et al., 2014; Cahyadi & Heki, 2015) and the correlation of directivity between ground vibrations and Rayleigh wave-induced CID has been confirmed (H. Liu et al., 2017). The CID first appeared in the south area of the epicenter and propagated to the south far-field outward from the epicenter, while no obvious CID can be detected in the north region of the epicenter. This result is consistent with previous works, i.e., the 2003 Tokachi-Oki earthquake (Rolland et al., 2011), the 2008 Wenchuan earthquake (Zhao & Hao, 2015) and the 2012 Haida Gwaii earthquake (Jin, Jin, & Li, 2017). Because, previous works have shown that the plasma waves cannot propagate perpendicularly to MF lines and CID propagating to equatorward is at smaller angles with MF line and favorable to be detected for long disturbance (Astafyeva et al., 2014; Bagiya et al., 2019; Heki & Ping, 2005). The 2020 Jamaica earthquake occurred in the northern hemisphere, and the detailed information about the geomagnetic field near the epicenter area was obtained using the IGRF model from National Oceanic and Atmospheric Administration (NOAA, <https://www.ngdc.noaa.gov>). The geomagnetic field has a westerly declination around 6.40°, and a downward inclination around 47.65° at the ionosphere height of 350 km. Therefore, the Rayleigh-induced

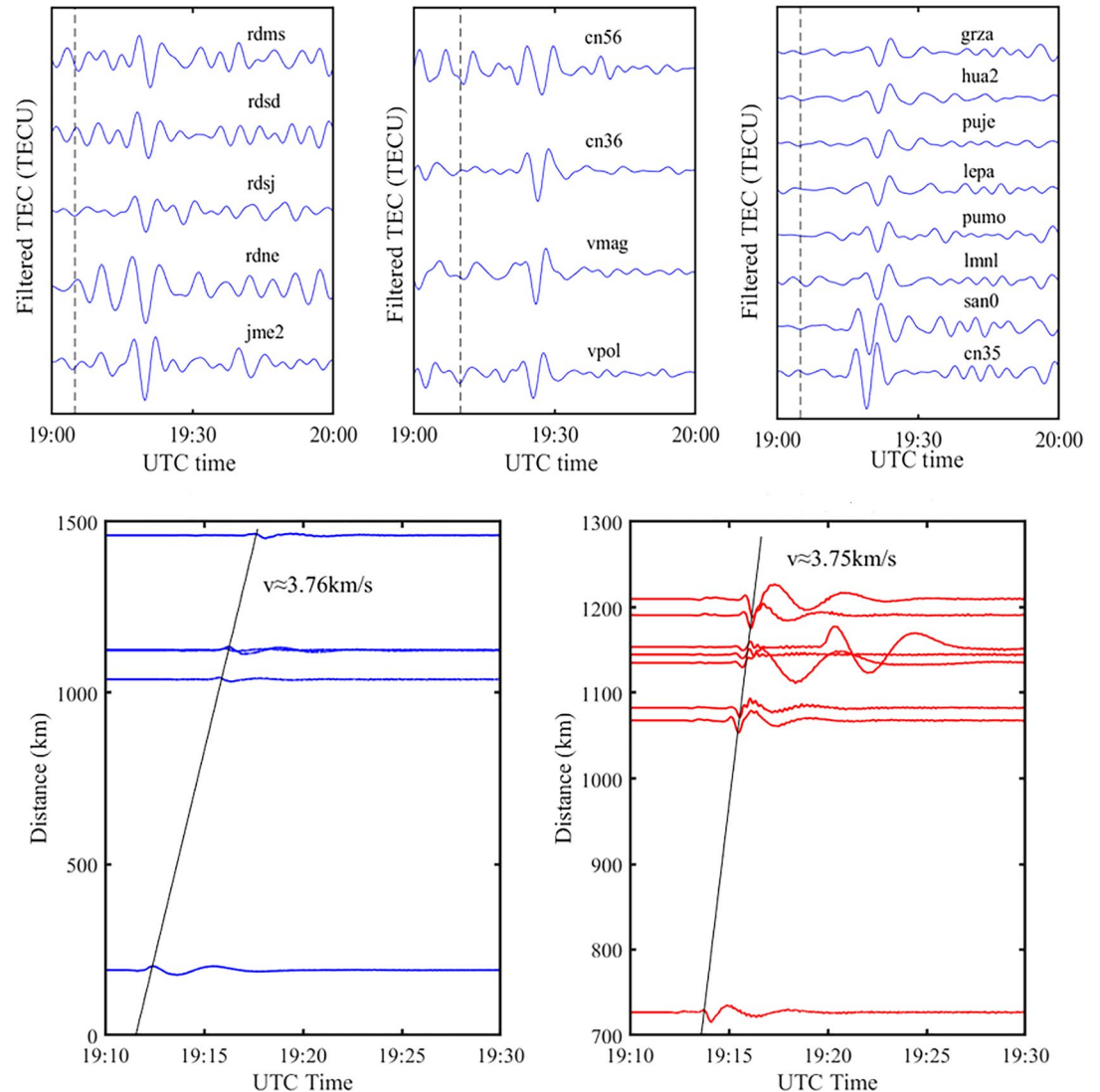


Figure 7. (a) Disturbance waveforms from observations of selected stations for PRN03. (b) Disturbance waveforms from observation of selected stations for PRN04. (c) Disturbance waveforms from observation of selected stations for PRN26. (d) Seismic waves in southeast direction. (e) Seismic waves in southwest direction.

disturbance wave vector in the south area of epicenter propagates at small angles (less than 30°) to the MF line and can be easily detected from GPS observation.

As is mentioned in Figure 1b, the fault rupture was located at the epicentral azimuth 258° and the rupture propagation direction was mainly along westward direction (Tira et al., 2020). Besides, the vertical ground displacements shown in Figures 7d and 7e demonstrate that the southwest area has larger ground displacements than southeast area. These facts corroborate the larger ground deformation and energy propagation in the west and southwest of the epicenter. Due to the decreasing background air density, the amplitudes of CID grow exponentially with the altitude to conserve energy when the acoustic waves propagate upward into the atmosphere (Meng et al., 2019). Therefore, the CID with propagation along the southwest direction will have a more intense ionospheric response and larger amplitude after amplification. On the other hand, the non-tectonic forcing mechanisms, such as satellite geometry, should be considered. However, the elevation angles of satellite PRN03, 04 and 26 are all at low angle range, which may have less impact on the amplitude of CID. Moreover, Zhao and Hao (2015) found two groups of CIDs with maximum amplitudes in the direction of azimuth 150° and 135° following the 2008 Wenchuan earthquake, which are perpendicular

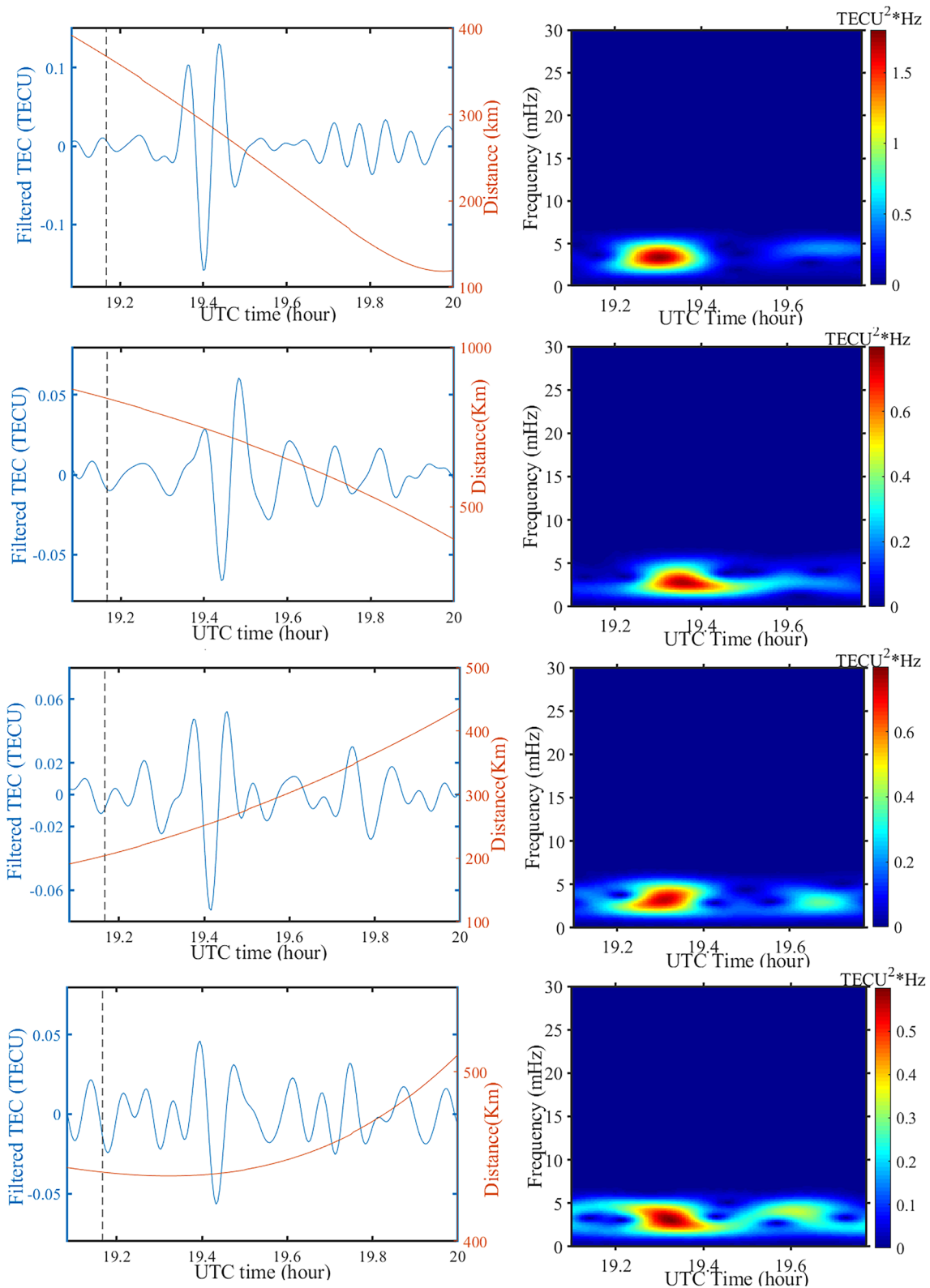


Figure 8. The spectrograms of TEC disturbances series from selected stations and satellites. (a) Station CN35 for satellite PRN26. (b) Station GRZA for satellite PRN26. (c) Station JME2 for satellite PRN03. (d) Station RDMS for satellite PRN03.

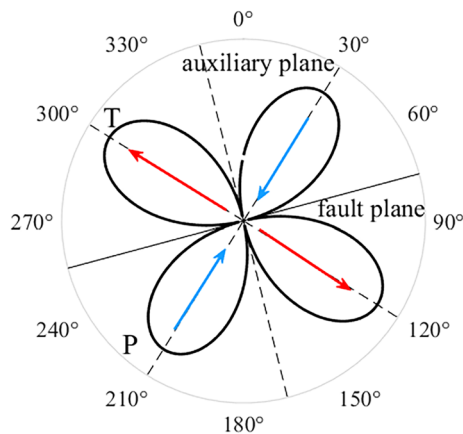


Figure 9. Schematic diagram for focal mechanism. Specific factors are obtained from (<https://earthquake.usgs.gov/earthquakes/eventpage/pt20028001/moment-tensor>).

to the direction of the fault rupture. However, as the 2020 Jamaica earthquake has a different focal mechanism, the maximum amplitudes of CIDs concentrate on the direction of azimuth 200–240°, which are close to the direction of the fault rupture (258°, shown in Figure 1b). For another example, the 2012 Haida Gwaii earthquake, CID propagates toward southeast direction, which is parallel to the fault rupture direction (Jin, Jin, & Li, 2017). The directivity relation between CID and fault rupture may be determined by specific focal mechanism.

The disturbance signals display in the forms of inverted N-shape wave and typical N-shape wave. Several CID signal waveforms show the same polarity with generation source waves (Rayleigh waves). This demonstrates that CIDs appear in different initial polarities may attribute to different ground-motion patterns. Astafyeva and Heki (2009) suggested that the waveform of disturbance signals repeat the initial ground crustal motion and may contain the information about the focal mechanism (Heki et al., 2006). The typical and inverse N-shape wave are caused by mixed type of focal mechanism. This view can be supported from previous earthquake cases. For instance, Jin, Jin, and Li (2017) investigated the CID following the 2012 Haida Gwaii earthquake through dual-frequency

GPS observation. The Rayleigh wave-induced CID showed a negative initial polarity, which was similar to the polarity of waves recorded by the seismic station and bottom pressure records in the seafloor. Moreover, Catherine et al. (2015) analyzed the ionospheric response following the 2012 Indian Ocean strike-slip earthquake using GPS-TEC measurements. Results suggest that TEC waveforms were mostly consistent with the focal mechanism of the earthquake.

Besides, according to Sipkin (1994) and Kiratzi (2014), the focal mechanism illustrates the pattern of the radiated seismic waves and can be determined by the first motion polarity of the body and surface wave. Figure 9 represents the schematic diagram for focal mechanism. The specific information about focal mechanism was obtained from USGS (<https://earthquake.usgs.gov/earthquakes/eventpage/pt20028001/moment-tensor>). The P-axis, T-axis, fault plane and auxiliary plane are labeled in the diagram. The origin represents the hypocenter and the theta axis shows the epicenter azimuths (in degree). It indicates that during the slip, the southwest quadrant of the fault is a compression region while the southeast quadrant can be considered as a dilatation or extension region. Thus, the appearance of inverted N-shaped waves in the southwest area detected by PRN26 may attribute to the negative co-seismic vertical crustal movement, and the typical N-shape waves detected in the near-field southeast area ascribes to the co-seismic vertical ground uplift. The ground movement pattern matches the Rayleigh waves shown in Figures 7d and 7e.

However, Rolland et al. (2013) argued that the amplitude and waveform of TEC signals may be controlled by other factors, such as geomagnetic field, geometry of the GPS line-of-sight signal and background ionization as well as geological structure (e.g., Tenzer et al., 2015). The dependence of waveform of near-field CIDs on focal mechanisms can only be done in the regions where the geomagnetic field hardly distorts the ionospheric response (Astafyeva & Heki, 2009). However, different from Rolland et al. (2013), the inverted N-shaped wave and N-shaped wave are both appear in the south area of epicenter, where the MF line has moderate impact on the CID waves. As the absence of displacement and waveform data of seafloor in the near-field area, further investigation is necessary to determine the formation of the inverted N-shaped wave.

4. Summary

The ionospheric responses to the 2020 M_w 7.7 Jamaica earthquake were studied and estimated by dense dual-frequency GPS measurements. The CIDs are mainly captured by Satellite PRN03, PRN04 and PRN26 after about 12 min of the main shock in the south near-field area, which is 300–500 km away from the epicenter and the southwest far-field area, which is 800 km away from the epicenter. The propagation velocity of CIDs observed from PRN03, PRN04 and PRN26 are 3.54 km/s, 3.51 km/s and 3.48 km/s, respectively. The variation amplitudes of the disturbances detected by PRN26 are larger than PRN03's and PRN04's. The

average variation amplitude of the disturbances detected by PRN26 is larger than -0.08 TECU, while the PRN03's reaches only to -0.05 TECU and PRN04's reaches to -0.07 TECU. The azimuthal asymmetry in amplitude of filtered TEC series mainly attributes to the fault system and the spread distribution of earthquake energy. Besides, the center frequencies of the co-seismic ionospheric disturbances signals detected by PRN26 are about 3.4 and 3.0 mHz, while the disturbances signals detected by PRN03 are centered at 3.3 and 3.1 mHz. These disturbance signals all belong to infrasonic waves. Furthermore, the ionospheric disturbances are the secondary acoustic waves in the infrasonic frequency range induced by the seismic Rayleigh surface wave with dynamic coupling. The similar directivity and initial polarity between ground motion and Rayleigh wave-induced CID will help comprehend the correlation and coupling mechanism of CID and earthquake, but it should be further studied from more earthquake cases in the future.

Data Availability Statement

Great gratitude to UNAVCO (<https://www.unavco.org/data/data.html>) for providing the GPS observation data, IRIS Data Management Center (<http://ds.iris.edu/ds/>) for seismograph data and NOAA (<https://www.ngdc.noaa.gov/geomag/calculators/magcalc.shtml#igrfwm>) for providing geomagnetic field information.

Acknowledgments

This work was supported by the National Natural Science Foundation of China (NSFC) Project (Grant No. 12073012) and National Natural Science Foundation of China-German Science Foundation (NSFC-DFG) Project (Grant No. 41761134092).

References

- Afraimovich, E. L., Ding, F., Kiryushkin, V. V., Astafyeva, E. I., Jin, S., & Sankov, V. A. (2010). TEC response to the 2008 Wenchuan Earthquake in comparison with other strong earthquakes. *International Journal of Remote Sensing*, *31*(13), 3601–3613. <https://doi.org/10.1080/01431161003727747>
- Afraimovich, E. L., Palamartchouk, K. S., & Perevalova, N. P. (1998). GPS radio interferometry of traveling ionospheric disturbances. *Journal of Atmospheric and Solar-Terrestrial Physics*, *60*(12), 1205–1223. <https://doi.org/10.1016/j.asr.2016.11.001>
- Afraimovich, E. L., Perevalova, N. P., Plotnikov, A. V., & Uralov, A. M. (2001). The shock-acoustic waves generated by the earthquakes. *Annales Geophysicae*, *19*(4), 395–409. <https://doi.org/10.5194/angeo-19-395-2001>
- Astafyeva, E. (2019). Ionospheric detection of natural hazards. *Review of Geophysics*, *57*(4), 1265–1288. <https://doi.org/10.1029/2019RG000668>
- Astafyeva, E., & Heki, K. (2009). Dependence of waveform of near-field coseismic ionospheric disturbances on focal mechanisms. *Earth Planets and Space*, *61*(7), 939–943. <https://doi.org/10.1186/BF03353206>
- Astafyeva, E., Heki, K., Kiryushkin, V., Afraimovich, E., & Shalimov, S. (2009). Two-mode long-distance propagation of coseismic ionosphere disturbances. *Journal of Geophysical Research*, *114*, A10307. <https://doi.org/10.1029/2008JA013853>
- Astafyeva, E., Rolland, L. M., & Sladen, A. (2014). Strike-slip earthquakes can also be detected in the ionosphere. *Earth and Planetary Science Letters*, *405*, 180–193. <https://doi.org/10.1016/j.epsl.2014.08.024>
- Astafyeva, E., Shalimov, S., Olshanskaya, E., & Lognonné, P. (2013). Ionospheric response to earthquakes of different magnitudes: Larger quakes perturb the ionosphere stronger and longer. *Geophysical Research Letters*, *40*, 1675–1681. <https://doi.org/10.1002/grl.50398>
- Bagiya, M. S., Sunil, A. S., Rolland, L., Nayak, S., Ponraj, M., Thomas, D., & Ramesh, D. S. (2019). Mapping the impact of non-tectonic forcing mechanisms on GNSS measured coseismic ionospheric perturbations. *Scientific Reports*, *9*, 18640. <https://doi.org/10.1038/s41598-019-54354-0>
- Brunini, C., & Azpilicueta, F. J. (2009). Accuracy assessment of the GPS-based slant total electron content. *Journal of Geodesy*, *83*(8), 773–785. <https://doi.org/10.1007/s00190-008-0296-8>
- Cahyadi, M. N., & Heki, K. (2015). Coseismic ionospheric disturbance of the large strike-slip earthquakes in North Sumatra in 2012: Mw dependence of the disturbance amplitudes. *Geophysical Journal International*, *200*(1), 116–129. <https://doi.org/10.1093/gji/ggu343>
- Cai, C., Liu, Z., Xia, P., & Dai, W. (2013). Cycle slip detection and repair for undifferenced GPS observations under high ionospheric activity. *GPS Solutions*, *17*, 247–260. <https://doi.org/10.1007/s10291-012-0275-7>
- Calais, E., & Minster, J. B. (1995). GPS detection of ionospheric perturbations following the January 17, 1994, Northridge earthquake. *Geophysical Research Letters*, *22*(9), 1045–1048. <https://doi.org/10.1029/95GL00168>
- Catherine, J. K., Vijayan, M. S. M., Syeda Rabiya, U. B., Shimna, K., Gahalaut, V. K., & Ramesh, D. S. (2015). Dichotomy in mode propagation of coseismic ionospheric disturbance: Observations from 11 April 2012 Indian Ocean earthquake. *Journal of Geophysical Research*, *120*(5), 3854–3867. <https://doi.org/10.1002/2014JA020621>
- Davies, K., D. M. Baker, (1965). Ionospheric effects observed around the time of the Alaskan earthquake of March 28, 1964. *Journal of Geophysical Research*, *70*(9), 2251–2253. <https://doi.org/10.1029/JZ070i009p02251>
- Ducic, V., Artru, J., & Lognonné, P. (2003). Ionospheric remote sensing of the Denali Earthquake Rayleigh surface waves. *Geophysical Research Letters*, *30*(18), 1951. <https://doi.org/10.1029/2003GL017812>
- Heki, K., Otsuka, Y., Choosakul, N., Hemmakorn, N., Komolmis, T., & Maruyama, T. (2006). Detection of ruptures of Andaman fault segments in the 2004 Great Sumatra Earthquake with coseismic ionospheric disturbances. *Journal of Geophysical Research*, *111*. <https://doi.org/10.1029/2005JB004202>
- Heki, K., & Ping, J. S. (2005). Directivity and apparent velocity of the coseismic ionospheric disturbances observed with a dense GPS array. *Earth and Planetary Science Letters*, *236*, 845–855. <https://doi.org/10.1016/j.epsl.2005.06.010>
- Jin, S. G. (2018). Two-mode ionospheric disturbances following the 2005 Northern California offshore earthquake from GPS measurements. *Journal of Geophysical Research*, *123*, 8587–8598. <https://doi.org/10.1029/2017JA025001>
- Jin, S. G., Han, L., & Cho, J. (2011). Lower atmospheric anomalies following the 2008 Wenchuan Earthquake observed by GPS measurements. *Journal of Atmospheric and Solar-Terrestrial Physics*, *73*(7–8), 810–814. <https://doi.org/10.1016/j.jastp.2011.01.023>
- Jin, S. G., Jin, R., & Kutoglu, H. (2017). Positive and negative ionospheric responses to the March 2015 geomagnetic storm from BDS observations. *Journal of Geodesy*, *91*(6), 613–626. <https://doi.org/10.1007/s00190-016-0988-4>
- Jin, S. G., Jin, R., & Li, D. (2017). GPS detection of ionospheric Rayleigh wave and its source following the 2012 Haida Gwaii earthquake. *Journal of Geophysical Research*, *122*(1), 1360–1372. <https://doi.org/10.1002/2016JA023727>

- Jin, S. G., Occhipinti, G., & Jin, R. (2015). GNSS ionospheric seismology: Recent observation evidences and characteristics. *Earth-Science Reviews*, 147, 54–64. <https://doi.org/10.1016/j.earscirev.2015.05.003>
- Jin, S. G., & Park, P. H. (2006). Strain accumulation in South Korea inferred from GPS measurements. *Earth Planets and Space*, 58(5), 529–534. <https://doi.org/10.1186/BF03351950>
- Jin, S. G., & Su, K. (2020). PPP models and performances from single- to quad-frequency BDS observations. *Satellite Navigation*, 1(1), 16. <https://doi.org/10.1186/s43020-020-00014-y>
- Jin, S. G., Wang, J., Zhang, H., & Zhu, W. Y. (2004). Real-time monitoring and prediction of the total ionospheric electron content by means of GPS observations. *Chinese Journal of Astronomy and Astrophysics*, 28(3), 331–337. <https://doi.org/10.1016/j.chinastron.2004.07.008>
- Kiratzis, A. A. (2014). Mechanism of earthquake in Aegean. *Encyclopedia of Earthquake Engineering*, 4, 3966.
- Komjathy, A., Yang, Y. M., Meng, X., Verkhoglyadova, O., Mannucci, A. J., & Langley, R. B. (2016). Review and perspectives: Understanding natural-hazards-generated ionospheric perturbations using GPS measurements and coupled modeling. *Radio Science*, 51(7), 951–961. <https://doi.org/10.1002/2015RS005910>
- Leonard, R. S., & Barnes, R. A., JR (1965). Observation of ionospheric disturbances following the Alaska Earthquake. *Journal of Geophysical Research*, 70(5), 1250–1253. <https://doi.org/10.1029/JZ070i005p01250>
- Liu, H., Ding, F., Zhao, B., Li, J., Hu, L., Wan, W., & Ning, B. (2017). Ionospheric response following the Mw 7.8 Gorkha earthquake on 25 April 2015. *Journal of Geophysical Research: Space Physics*, 122, 6495–6507. <https://doi.org/10.1002/2016JA023079>
- Liu, H., Zhang, K. K., Imtiaz, N., Song, Q., & Zhang, Y. (2021). Relating far-field coseismic ionospheric disturbances to geological structures. *Journal of Geophysical Research: Space Physics*, 126(7). <https://doi.org/10.1029/2021JA029209>
- Liu, J. Y., Chen, C. H., Lin, C. H., Tsai, H.-F., Chen, C.-H., & Kamogawa, M. (2011). Ionospheric disturbances triggered by the 11 March 2011 M 9.0 Tohoku earthquake. *Journal of Geophysical Research*, 116, A06319. <https://doi.org/10.1029/2011JA016761>
- Meng, X., Vergados, P., Komjathy, A., & Verkhoglyadova, O. (2019). Upper atmospheric responses to surface disturbances: An observational perspective. *Radio Science*, 54(11), 1076–1098. <https://doi.org/10.1029/2019RS006858>
- Nguyen, V. K., Rovira-Garcia, A., Juan, J. M., Sanz, J., González-Casado, G., La, T. V., & Ta, T. H. (2019). Measuring phase scintillation at different frequencies with conventional GNSS receivers operating at 1 Hz. *Journal of Geodesy*, 93, 1985–2001. <https://doi.org/10.1007/s00190-019-01297-z>
- Occhipinti, G., Dorey, P., Farges, T., & Lognonné, P. (2010). Nostradamus: The radar that wanted to be a seismometer. *Geophysical Research Letters*, 37, L18104. <https://doi.org/10.1029/2010GL044009>
- Okoh, D., Onwuneme, S., Seemala, G., Jin, S. G., Rabiou, B., Nava, B., & Uwamahoro, J. (2018). Assessment of the NeQuick-2 and IRI-Plas 2017 models using global and long-term GNSS measurements. *Journal of Atmospheric and Solar-Terrestrial Physics*, 170, 1–10. <https://doi.org/10.1016/j.jastp.2018.02.006>
- Peravalova, N. P., Sankov, V. A., Astafyeva, E., & Zhupityaeva, A. S. (2014). Threshold magnitude for ionospheric response to earthquakes. *Journal of Atmospheric and Solar-Terrestrial Physics*, 108, 77–90. <https://doi.org/10.1016/j.jastp.2013.12.014>
- Rolland, L. M., Lognonné, P., & Munekane, H. (2011). Detection and modeling of Rayleigh wave induced patterns in the ionosphere. *Journal of Geophysical Research: Space Physics*, 116, 1–18. <https://doi.org/10.1029/2010JA016060>
- Rolland, L. M., Occhipinti, G., Lognonné, P., & Loevenbruck, A. (2010). Ionospheric gravity waves detected offshore Hawaii after tsunamis. *Geophysical Research Letters*, 37. <https://doi.org/10.1029/2010GL044479>
- Rolland, L. M., Vergnolle, M., Nocquet, J. M., Sladen, A., Dessa, J. X., Tavakoli, F., et al. (2013). Discriminating the tectonic and non-tectonic contributions in the ionospheric signature of the 2011, Mw 7.1, dip-slip van earthquake, eastern Turkey. *Geophysical Research Letters*, 40, 2518–2522. <https://doi.org/10.1002/grl.50544>
- Ronald, V. R. (1966). Evidence of Long-Period Acoustic-Gravity Waves Launched into the F region by the Alaskan. *Journal of Geophysical Research*, 71(1), 343–345. <https://doi.org/10.1029/jz071i001p00343>
- Ronald, V. R. (1967). Acoustic-gravity waves in the upper atmosphere due to a nuclear detonation and an earthquake. *Journal of Geophysical Research*, 72(5), 1599–1610. <https://doi.org/10.1029/JZ072i005p01599>
- Saito, A., Tsugawa, T., Otsuka, Y., Nishioka, M., Iyemori, T., Matsumura, M., et al. (2011). Acoustic resonance and plasma depletion detected by GPS total electron content observation after the 2011 off the Pacific coast of Tohoku earthquake. *Earth Planets and Space*, 63(7), 863–867. <https://doi.org/10.5047/eps.2011.06.034>
- Sipkin, S. A. (1994). Rapid determination of global moment-tensor solutions. *Geophysical Research Letters*, 21(16), 1667–1670. <https://doi.org/10.1029/94GL01429>
- Sripathi, S., Singh, R., Tiwari, P., & Kumar, M. R. (2020). On the co-seismic ionospheric disturbances (CIDs) in the rapid run ionosonde observations over Allahabad following Mw 7.8 Nepal Earthquake on April 25, 2015. *Journal of Geophysical Research*, 125, 2169–2185. <https://doi.org/10.1029/2019JA027001>
- Tenzer, R., Chen, W., & Jin, S. G. (2015). Effect of the upper mantle density structure on the Moho geometry. *Pure and Applied Geophysics*, 172(6), 1563–1583. <https://doi.org/10.1007/s00024-014-0960-2>
- Tira, T., Okuwaki, R., Yagi, Y., & Yamashita, S. (2020). Rupture process of the 2020 Caribbean Earthquake along the oriente transform fault, involving supershear rupture and geometric complexity of fault. *Geophysical Research Letters*, 48(1). <https://doi.org/10.1029/2020GL090899>
- Tsugawa, T., Saito, A., Otsuka, Y., Nishioka, M., Maruyama, T., Shinagawa, H., et al (2011). *Ionospheric disturbances detected by GPS total electron content observation after the 2011 Tohoku earthquake*. AGU Fall Meeting Abstracts.
- Zhao, B., & Hao, Y. (2015). Ionospheric and geomagnetic disturbances caused by the 2008 Wenchuan earthquake: A revisit. *Journal of Geophysical Research: Space Physics*, 120, 5758–5777. <https://doi.org/10.1002/2015JA021035>